Acousto-optic cavity coupling in 2D phoxonic crystal with combined convex and concave holes

Jun Jin, Shan Jiang, Hongping Hu, et al.

View Online   Export Citation   CrossMark

ARTICLES YOU MAY BE INTERESTED IN

Unified potential fluctuations model for photoluminescence spectra at room temperature—Cu(In,Ga)Se$_2$ thin films
Journal of Applied Physics 130, 123103 (2021); https://doi.org/10.1063/5.0056629

A practical guide to modeling low-current quasi-stationary gas discharges: Eigenvalue, stationary, and time-dependent solvers
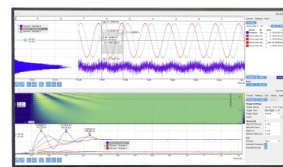Journal of Applied Physics 130, 121101 (2021); https://doi.org/10.1063/5.0057856

Influence of solution electrical conductivity and ionic composition on the performance of a gas–liquid pulsed spark discharge reactor for water treatment
Journal of Applied Physics 130, 123301 (2021); https://doi.org/10.1063/5.0054327

Acousto-optic cavity coupling in 2D phoxonic crystal with combined convex and concave holes

View Online   Export Citation   CrossMark

Jun Jin,[1,2] Shan Jiang,[1,3] Hongping Hu,[1,2,a] Lamin Zhan,[4] Xiaohong Wang,[4] and Vincent Laude[5]

AFFILIATIONS

[1]Department of Mechanics, School of Aerospace Engineering, Huazhong University of Science and Technology, Wuhan 430074, People's Republic of China
[2]Hubei Key Laboratory of Engineering Structural Analysis and Safety Assessment, Huazhong University of Science and Technology, Wuhan 430074, People's Republic of China
[3]State Key Laboratory of Digital Manufacturing Equipment and Technology, Huazhong University of Science and Technology, Wuhan 430074, People's Republic of China
[4]School of Optical and Electronic Information, Huazhong University of Science and Technology, Wuhan 430074, People's Republic of China
[5]Franche-Comté Electronique Mécanique Thermique et Optique, CNRS UMR 6174, Université de Bourgogne Franche-Comté, Besançon 25030, France

[a]Author to whom correspondence should be addressed: huhp@hust.edu.cn

ABSTRACT

A two-dimensional cross-like phoxonic crystal (PxC) model is proposed, which exhibits simultaneously large complete photonic crystal (PtC) and phononic crystal (PnC) bandgaps. The most salient trait of the structure is the wide range of geometrical parameters compatible with large complete bandgaps. After geometrical optimization, photonic and phononic bandgaps with gap-to-midgap ratios of 11.5% and 90.7% are obtained, respectively. These values are close to the best topology-optimized reported values but are obtained with simple shapes compatible with nanoscale fabrication technology. These characteristics make the convex–concave topology a promising candidate for PxC devices. A cavity is then introduced by filling up one cross-like hole in the 7×7 super-cell. PtC and PnC bands with defects appear in the respective large complete bandgaps, confining phonons and photons in the same cavity. Acousto-optic (AO) coupling between photonic and phononic defect modes is further investigated by the finite element method, taking both photoelastic and moving interface mechanisms into consideration. The symmetries of both photonic and phononic modes play a dominant role in the coupling strength. Results show that the strongest linear coupling between a photonic transverse magnetic mode and phononic breathing mode is obtained due to the in-phase superposition in the x and y directions. A quadratic nonlinear coupling is observed when photonic modes are coupled with the phononic stretching mode due to the inverse superposition of x and y directions. Finally, the optomechanical coupling rates relative to zero-point motion are estimated.

I. INTRODUCTION

Because of their distinct advantages in enhancing acousto-optic interactions at the micro- and nanoscale, optomechanical[1–4] or phoxonic crystals (PxCs)[5–10] have attracted attention in recent years. Based on the combined concepts of PtCs[11] and PnCs,[12,13] PxCs introduce a spatial periodicity in both refractive index and acoustic impedance and then exhibit simultaneous photonic and phononic bandgaps. PxCs thus provide a systematic way into which point and linear defects can be engineered that break periodicity locally and give rise to cavities[5,6,14] and waveguides,[15,16] ultimately supporting the confinement and coupling of light and sound waves. In virtue of their unique traits, PxCs have become a powerful paradigm for optomechanical systems and acousto-optic devices.

A prerequisite for the simultaneous localization of light and sound is the presence of both photonic and phononic bandgaps, ideally complete, within which the propagation of light and sound

is forbidden whatever be the polarization and the wave vector. Compared with their 3D counterparts,[7] 1D and 2D PxCs have received the most attention since they are easier to model as well as to manufacture. We focus on 2D infinite PxCs in the following.

As observed in previous related works,[11,17] for the photonic bandgaps in the 2D case, connectivity of high-ε region (ε denotes dielectric permittivity) is conducive to transverse electric (TE) bandgaps, whereas isolated patches of high-ε regions lead to transverse magnetic (TM) bandgaps. For instance, TM bandgaps prefer lattices of airholes in a dielectric matrix and TE bandgaps favor lattices of dielectric columns in air. Therefore, the complete photonic bandgap is the result of a compromise between two conflicting objectives. On the other hand, for holey PnCs, heavy masses and slim connections are generally necessary for the unit cell to open a wide bandgap for both in-plane and out-of-plane modes.[18–21] As a whole, the optimal strategy of PxCs design is to find out a structure that possesses all these geometrical attributes or at least achieves a good balance between them.

One should also be aware of some obvious distinctions between PtCs and PnCs. For example, the triangular lattice of circular air columns in a dielectric matrix is not appropriate for the generation of phononic bandgaps, whereas it is the most widely used in PtC devices. As another example, the width of photonic bandgaps is conditioned by the contrast in the refractive index between the airholes and the matrix. The choice of material is hence vital for PtCs. The case of PnCs is different, however, since the presence of air can be neglected and elastic contrast is given by the traction-free boundaries of the holes. Such boundary conditions are independent of the choice of the material.

During the past few decades, many interesting PtCs and PnCs have been reported for efficiently modulating electromagnetic, acoustic, and elastic waves. The simultaneous existence of photonic and phononic bandgaps have also been disclosed in a variety of PxCs with different materials,[22–26] periodicity,[15,24] dimensions,[7,9,27–29] and topologies.[8,30–33] However, even though abundant types of PxCs have been considered in the literature, it is still a challenge to broaden simultaneously photonic and phononic bandgaps according to practical application demands. Because of technological constraints of fabrication at the micro- or nanoscale, the unit cell is quite often limited to a topology with simple shapes. A too complicated topology means that it could be difficult to fabricate even though the bandgaps are very wide. Moreover, other parameters like the tolerable amount of feature rounding and filet sizes are more important. Hence, the smallest feature width is extremely challenging even for cutting edge nano-fabrication techniques.

For two-dimensional (2D) PxCs, several works have reported the simultaneous existence of photonic and phononic bandgaps. Maldovan and Thomas[22] reported that phoxonic bandgaps can be obtained in a 2D square or hexagonal lattice crystals made of airholes in a silicon matrix. Sadat-Saleh et al.[23] and Bria et al.[24] reported the influence of the choice of lattice and filling fraction on bandgaps in 2D systems, considering LiNbO$_3$ (lithium niobate) for the former and sapphire/silicon for the later. Recently, Dong et al.[31] investigated the opening of phoxonic bandgaps by topology optimization. On the one hand, simple conventional topologies, like circular holes in a square lattice,[22–24] can hardly open large simultaneous bandgaps. On the other hand, topologies obtained from topology optimization are always complex and are quite difficult to manufacture, even though they theoretically achieve large simultaneous bandgaps.

In a recent work, we proposed a convex–concave combination in a 2D square lattice PnC with a cross-like hole in the center of the unit cell surrounded by four square holes at the corners,[21] whose most notable advantage is the generation of ultra-wide bandgaps in such a simple topology. In this work, we further investigate the optical characteristics of the convex–concave structure. A comprehensive search of complete dual bandgaps is conducted. In addition to the broad phononic bandgaps, large photonic bandgaps are also identified. The optimal gap-to-midgap ratios for the complete photonic and phononic bandgaps are 11.5% and 90.7%, respectively. In summary, the following advantages of the proposed PxC are demonstrated: (i) simultaneous broad complete photonic and phononic bandgaps and (ii) broad bandgaps that can be obtained in a wide range of geometrical parameters, which provide good tolerance for the technological realization and flexibility in designing. These traits are beneficial to improve feasibility, applicability, and reliability, making the proposed PxC as a potential candidate for practical applications.

Furthermore, with large complete bandgaps, the structure is suitable for AO devices due to the following two reasons: (i) More pure defect modes can be generated within the large bandgaps; (ii) Photonic defect modes are unlikely to move out of the bandgap even under strong AO coupling. Numerous approaches have been proposed to study AO interaction in phoxonic crystals with defects or cavities. The transfer matrix method[34] and the layer-multiple-scattering method[35] were employed to investigate 1D PxCs with defects. Transmittance and reflection of optical and acoustic defect modes were calculated to search the shift of optical defect frequency under AO coupling.[36] 1D PxCs with defects were also studied by a Born series approach with Green's function to derive the expression of the electric field.[36] It is worth noting that the first-order and second-order effects can be determined by first-order and second-order Born series, respectively. For 2D and 3D PxCs with cavities, the linear AO coupling rates of the photoelastic (PE) effect and the moving interface (MI) effect were obtained from the first-order perturbation theory.[6,37–39] The equation to obtain the quadratic AO coupling was given,[40] and the case of degenerate modes was further included.[41]

In optomechanics, the shift of the optical frequency is given by the product of the AO coupling rate and the zero-point fluctuation amplitude of the mechanical oscillator x_{zpf} that depends on both the effective mass and the acoustic frequency.[42] Obviously, the effective mass depends on the thickness of the structure. Hence, the results of the 2D model have to be compensated for by assuming a given thickness. Furthermore, in order to ensure the safety of the structure, a maximum strain in the cavity was limited to 1% or 0.1%. This can be achieved by setting the maximum modal displacement. Certainly, for PE and MI effects, the maximum mode displacement needs to be set the same in the calculation of optical frequency shift.

In this work, owing to the large complete bandgaps, the AO cavity coupling in the 2D PxC with combined convex and concave holes is further investigated. The AO couplings for the PE and the MI effects are studied by the first- and second-order perturbation

methods and the finite element method (FEM). An appropriate normalization on displacement is performed to estimate numerically the PE and the MI effects. Whether the acousto-optic coupling belongs to linear coupling or quadratic regime is further distinguished by FEM analysis. Moreover, optomechanical coupling rates relative to the zero-point motion are studied by 2D and 3D PxC models.

II. PXC MODEL AND THEORETICAL BASIS

As described in Fig. 1(b), a 2D square lattice PxC with a convex–concave topology is proposed by considering a cross-like hole in the center of the unit cell and four square convex holes at the corners. Alternatively, the structure can also be regarded as a central square surrounded by four L-shaped holes at the corners, as depicted in Fig. 1(c). In either case, the unit cell is formed by four lumps connected by four L-shaped connectors. Three independent parameters (b, c, d, or their derivatives) are required to determine the structure. The cross-like hole in the center is determined by b and c, while the side length of the square hole at each corner is $d/2$. The width of the connections is thus $h = (a - c - d)/2$. All these parameters are normalized against the lattice constant a in the following calculations. The chosen material is a single crystal silicon, with refractive index $n = 3.6$,[31] the mass density $\rho = 2320\ \text{kg/m}^3$, and the elastic constants

$c_{11} = 165.7$, $c_{12} = 64.1$, and $c_{44} = 79.6\ \text{GPa}$. Transverse and longitudinal speeds of sound are $c_t = 5840\ \text{m/s}$ and $c_l = 8433\ \text{m/s}$, respectively. The refractive index n of air in the holes is set to 1.

For electromagnetic waves propagating within the considered 2D infinite PxCs in the xy plane, Maxwell's equations can be decoupled into two scalar wave equations for transverse electric (TE) and transverse magnetic (TM) polarizations,[43,44]

$$\nabla^2 E_z(\mathbf{x}) + \left(\frac{\omega}{c_0}\right)^2 \varepsilon(\mathbf{x}) E_z(\mathbf{x}) = 0 \quad \text{for the TE mode,}$$

$$\nabla \cdot \left(\frac{1}{\varepsilon(\mathbf{x})} \nabla H_z(\mathbf{x})\right) + \left(\frac{\omega}{c_0}\right)^2 H_z(\mathbf{x}) = 0 \quad \text{for the TM mode,}$$

(1)

where ∇ is the gradient operator, ω denotes the angular frequency, and c_0 represents the speed of light in a vacuum. The distribution of the dielectric constant is periodic in the xy plane and uniform in the z direction. It satisfies $\varepsilon(\mathbf{x}) = \varepsilon(\mathbf{x} + \mathbf{a})$, where $\mathbf{x} = (x, y)$ is the position vector and $\mathbf{a}$ is a lattice vector. The electric and magnetic fields in the z direction E_z and H_z satisfy the Floquet–Bloch conditions $E_z(\mathbf{x} + \mathbf{a}) = \exp(i\mathbf{k} \cdot \mathbf{a}) E_k(\mathbf{x})$ and $H_z(\mathbf{x} + \mathbf{a}) = \exp(i\mathbf{k} \cdot \mathbf{a}) H_k(\mathbf{x})$. E_k and H_k are cell periodic fields and $\mathbf{k}$ is the Bloch wave vector restricted to the first Brillouin zone. "i" is the imaginary unit.
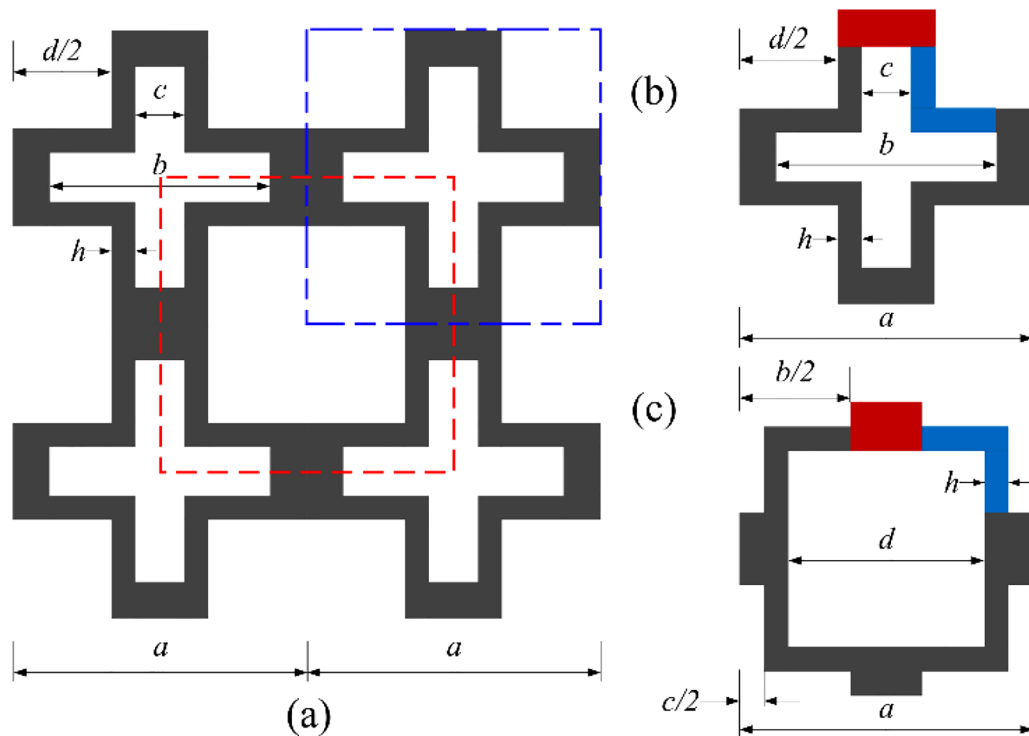

FIG. 1. Cross section of the proposed 2D square lattice PxC crystal: (a) an extended unit cell shows the arrangement of concave and convex holes; (b) and (c) show two possible equivalent primitive unit cells, as outlined by the blue and the red dotted lines in (a). In (b), the primitive cell is centered on the concave cross-like hole surrounded by four square holes placed at the corners. In (c), the primitive cell is centered on the convex square hole surrounded by four L-shaped holes placed at the corners. In (b) and (c), the red and blue areas both represent lumps and L-shaped connections.

Band structures are calculated by the finite element method (FEM). Floquet periodic boundary conditions are imposed on pairs of opposite external boundaries of the unit cell. All solutions are obtained by sweeping the wave vector **k** along the edges of the first irreducible Brillouin zone. In the band structures, normalized frequencies ($\omega a/2\pi c_0$ or $\omega a/2\pi c_t$) are functions of the reduced wave-number ($ka/2\pi$). The width of a bandgap can be measured using the gap-to-midgap ratio BG% = $200\%(f_{top} - f_{bot})/(f_{top} + f_{bot})$, a non-dimensional parameter that avoids frequency dependence, where

f_{top} and f_{bot} are the bounding frequencies of the bandgap. Generally, a higher BG% value means a better performance.

III. OPTIMIZED STRUCTURE FOR LARGE COMPLETE PHOXONIC BANDGAPS

Figures 2(a) and 2(b) depict phononic and photonic band structures for the proposed PxC, with geometrical parameters $b/a = 0.58$, $c/a = 0.32$, and $d/a = 0.62$. Large complete phononic
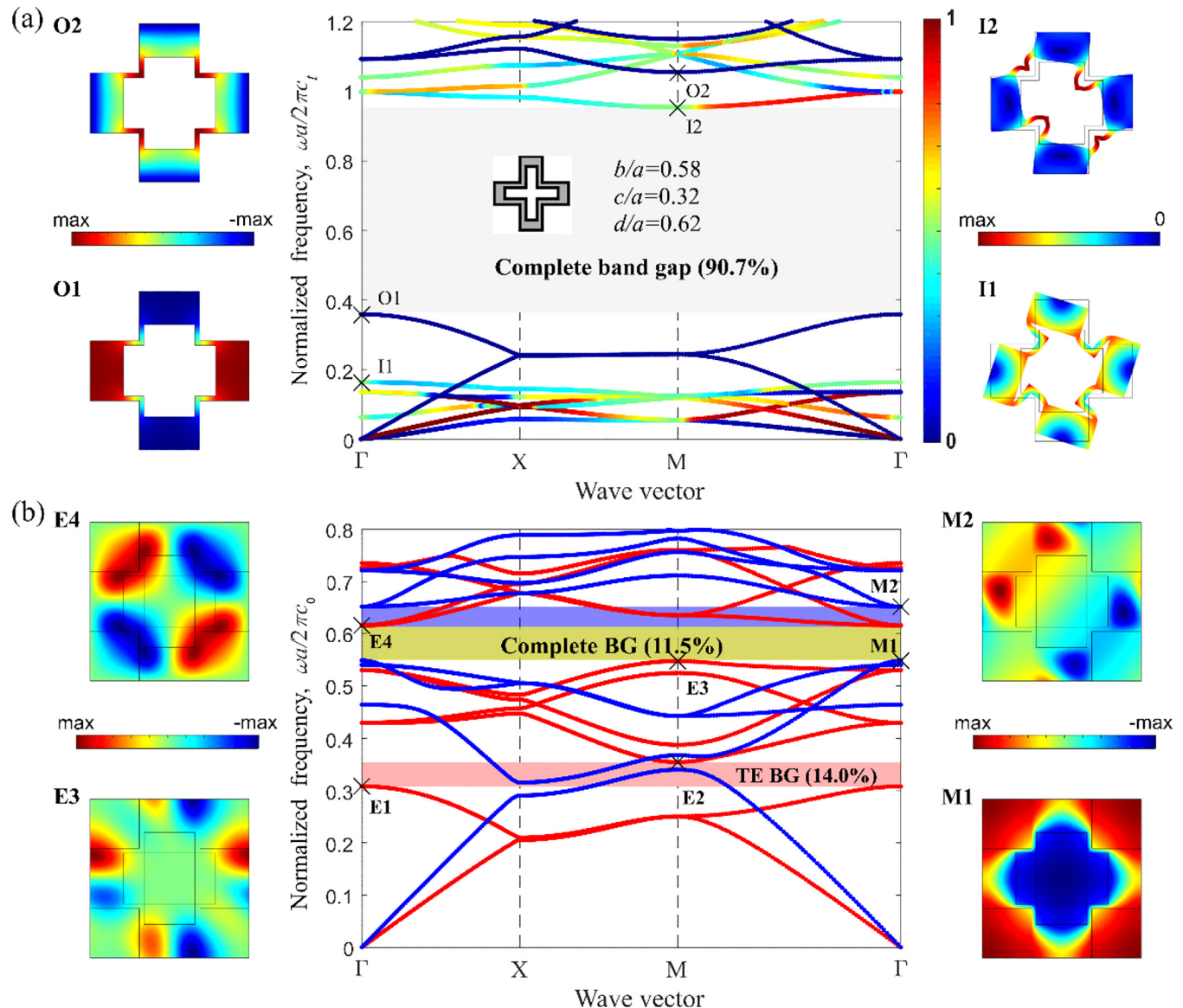

FIG. 2. (a) PnC and (b) PtC band structures of the proposed PxC and the corresponding eigenmodes at edges of the bandgaps, for parameters $b/a = 0.58$, $c/a = 0.32$, and $d/a = 0.62$. In (a), the color of bands represents the kinetic energetic ratio e_x of the x-polarization of the elastic wave. The blue curves represent bands of the out-of-plane mode, and the rest curves are bands of the in-plane mode. In (b), the blue and red lines denote the TM and TE polarizations, respectively.

(90.7%) and photonic (11.5%) bandgaps are visible. The complete photonic bandgap for normalized electromagnetic frequencies $\omega a/2\pi c_0$ ranges from 0.549 to 0.616, and the complete phononic bandgap for normalized elastic frequencies $\omega a/2\pi c_t$ is between 0.358 and 0.952. It is remarkable that although photonic and phononic bandgaps in PxCs occur at similar wavelengths of the order of twice the crystal periodicity a, the frequencies of the photonic and phononic gaps are very different since light and sound propagation velocities in solids differ by several orders of the magnitude. The dimensionless representation of the dispersion curve makes it easy to choose the lattice constant based on wavelength and frequency. For instance, if a PxC displays a photonic bandgap with midgap frequency at about 200 THz (telecom wavelength $\lambda = 1550$ nm), the lattice constant should be $a = 875$ nm. The midgap frequency of the phononic bandgap is then 4.39 GHz.

A comparison of dual complete bandgaps with published 2D PxCs is summarized in Table I to illustrate the advantages of the proposed topology. For each case, Table I lists the filling fraction of solid material, as well as the thickness of the connections h, which is the smallest feature limiting the fabrication. For clarify, except for the data directly quoted from Refs. 22 and 29, values are obtained considering silicon to facilitate comparison. Obviously, the proposed model has significant advantages over the first four types of PxCs regarding complete bandgaps.

For PnCs, the forming mechanism of large bandgaps with combined convex and concave holes was investigated previously.[20] Regarding PtCs, TM and TE polarizations need to be discussed separately. For the TM polarization, the magnetic energy of mode M1 is mainly confined within the vacuum holes (low-ε) regions. On the contrary, mode M2 is mainly concentrated in the solid dielectric (high-ε) regions. Therefore, for the adjacent modes, the dramatic change of the magnetic energy in the high-ε regions results in a large TM bandgap. For the TE polarization, the electric energy of both modes E3 and E4 distributes mostly in solid dielectric (high-ε) regions. However, mode E3 concentrates on lumps, whereas E4 concentrates on L-shape connections. Thus, the difference in the distribution of electric energy in the high-ε regions can explain the formation of a large TE bandgap. As a result, the upheaval of magnetic or electric fields in the high-ε regions between consecutive bands forms a bandgap. Moreover, a larger dielectric difference between regions opens a wider bandgap. This

result is in agreement with the previous idea that connectivity of high-ε regions is conducive to TM gaps, whereas isolated patches of high-ε regions lead to TE gaps.

A thorough geometrical optimization was carried out to reveal the relationship between bandgaps and geometrical parameters. Generally, it is preferable that the topology involves several geometrical parameters, offering more possibilities to tune bandgaps. For the proposed convex–concave PxC, three independent parameters need to be considered. We take b, c, and w ($w = a - 2h$) as those independent parameters. Parameter w is introduced as the void ratio in the x or y direction and is not shown in Fig. 1. The width of L-shaped connections h is critical for the generation of bandgaps and is the smallest feature size limiting fabrication. However, in order to display the geometric parameter range corresponding to the maximum bandwidth on the front view of Figs. 3(a) and 3(b), the ordinate represents w instead of h.

The effect of all geometrical parameters on phononic bandgaps are summarized in Fig. 3, in which the bandgap width BG% is displayed as a function of b/a, c/a, and w/a. Figures 3(a) and 3(b) present in-plane and out-of-plane modes, respectively. Hence, one can easily have an insight into the influence of each parameter and then their optimal combinations. Furthermore, ten slices taken for fixed parameter w/a are extracted from Figs. 3(a) and 3(b) and are shown in Figs. 3(c) and 3(d). Each slice demonstrates the dependence of bandgaps on b/a and c/a for a given w/a, by which one can understand variations more quantitatively and intuitively. At a glance, Fig. 3 reveals some interesting regularities. The first and perhaps most remarkable feature is that large bandgaps can exist over a wide range of parameters. In Figs. 3(a) and 3(b), two large bandgaps (BG% $\geq$ 130% and BG% $\geq$ 90%) appear as the two big red kernels. Second, bandgaps for out-of-plane modes are mostly contained in the bandgaps for in-plane modes, resulting in large complete phononic bandgaps. Third, each parameter affects similarly in-plane and out-of-plane bandgaps. More specifically, BG% peaks at an intermediate value of b/a and decreases as b/a deviates from this value when the other parameters are fixed, and a similar trend is observed with c/a. However, BG% increases with w/a.

The same analysis was performed for photonic bandgaps. The results are displayed in Fig. 4. Figures 4(a) and 4(b) show the results for TM and TE polarizations, respectively. Figures 4(c) and 4(d) display similar slices as in Figs. 3(c) and 3(d). Compared

TABLE I. Comparison of maximum relative bandgap widths for the proposed model and some published structures. h denotes the smallest size and V_f is the filling fraction of the solid material.

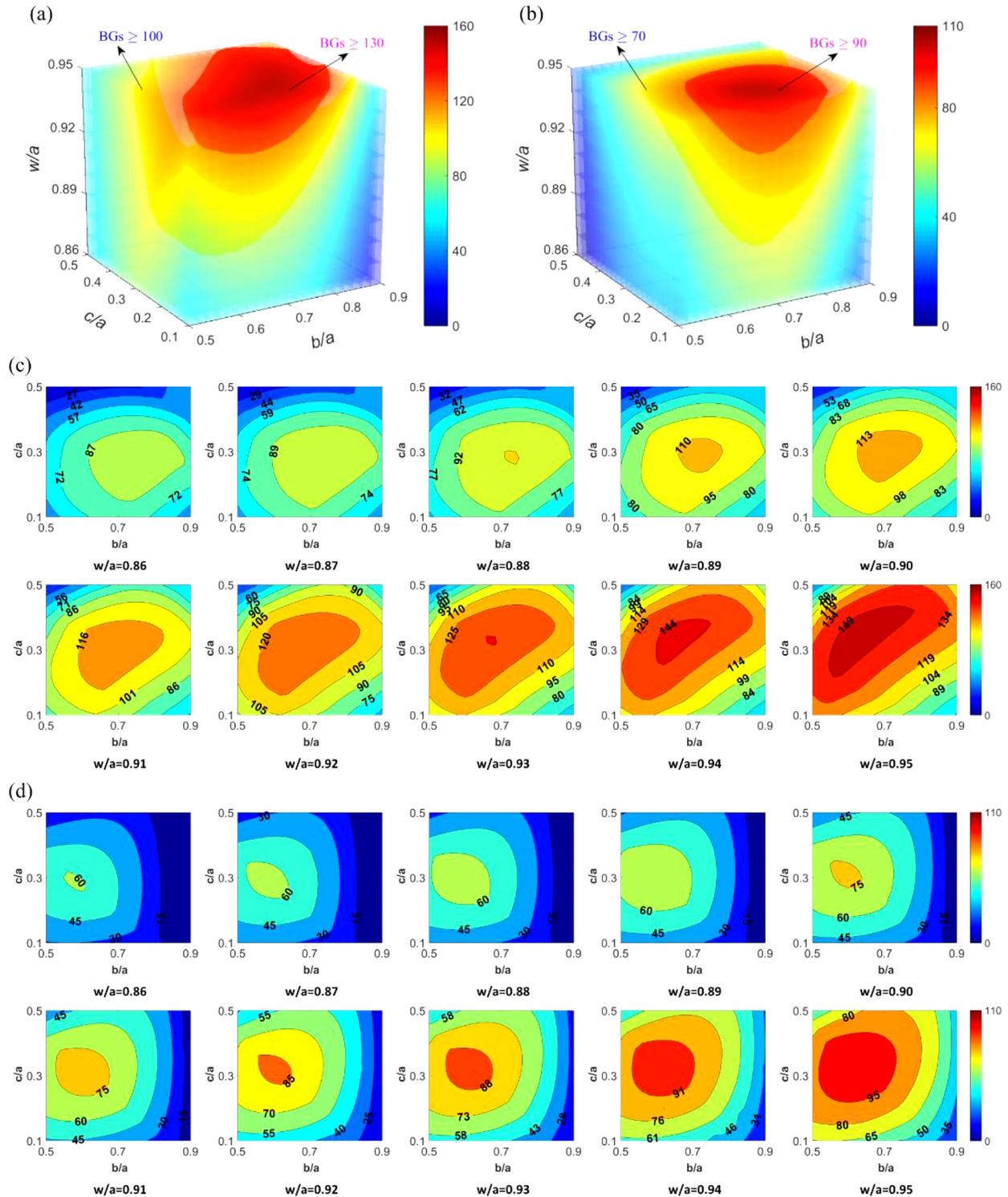| PxCs | h/a | Complete BG% | | V_f |
		PnC (%)	PtC (%)	
Square lattice of circular airholes[22]	1/40	44.5	No complete bandgaps	0.292
Triangular lattice[11]	0.01	No complete bandgaps	3.93	0.360
Honeycomb lattice[23]	<0.01	69.9	No complete bandgaps	n.a.
Ref. 24	1/25	38.1	8.32	0.336
Dielectric circles connected by veins[30]	0.03	83.8	11.3	0.307
Topology optimization[31]	n.a.	94.2	14.7	>0.5
This work	0.03	90.7	11.5	0.347

FIG. 3. The effect of geometrical parameters on (a) in-plane and (b) out-of-plane bandgaps, where BG% is illustrated by color as a function of *b/a*, *c/a*, and *w/a*. (c) and (d) are slices extracted from (a) and (b), respectively, and each slice demonstrates the influence of *b/a* and *c/a* on the bandgaps for a given *w/a*.

FIG. 4. The effect of geometrical parameters on (a) TM and (b) TE bandgaps, where BG% is illustrated by color as a function of *b/a*, *c/a*, and *w/a*. (c) and (d) are slices extracted from (a) and (b), respectively, and each slice demonstrates the influence of *b/a* and *c/a* on the bandgaps for a given *w/a*.
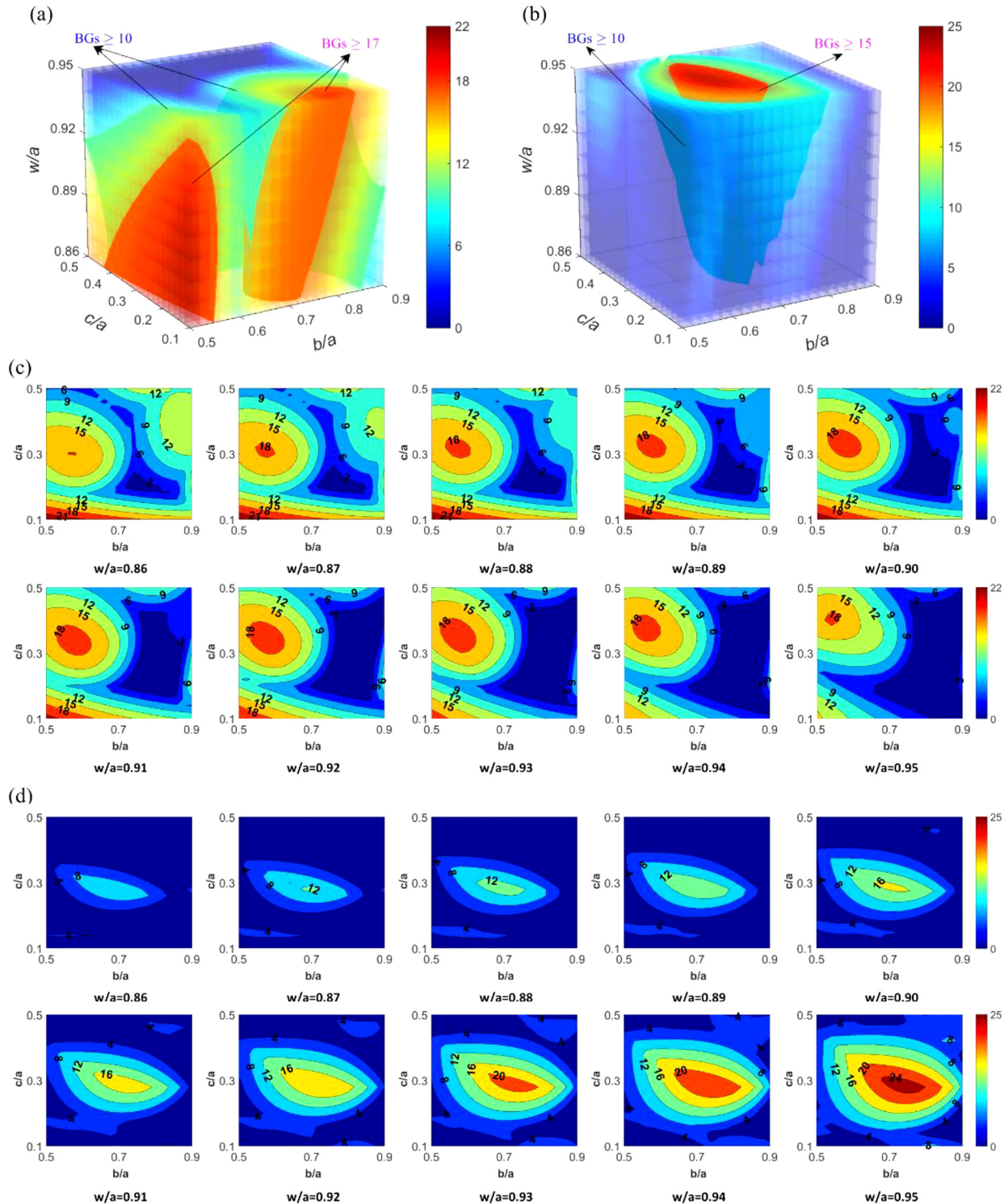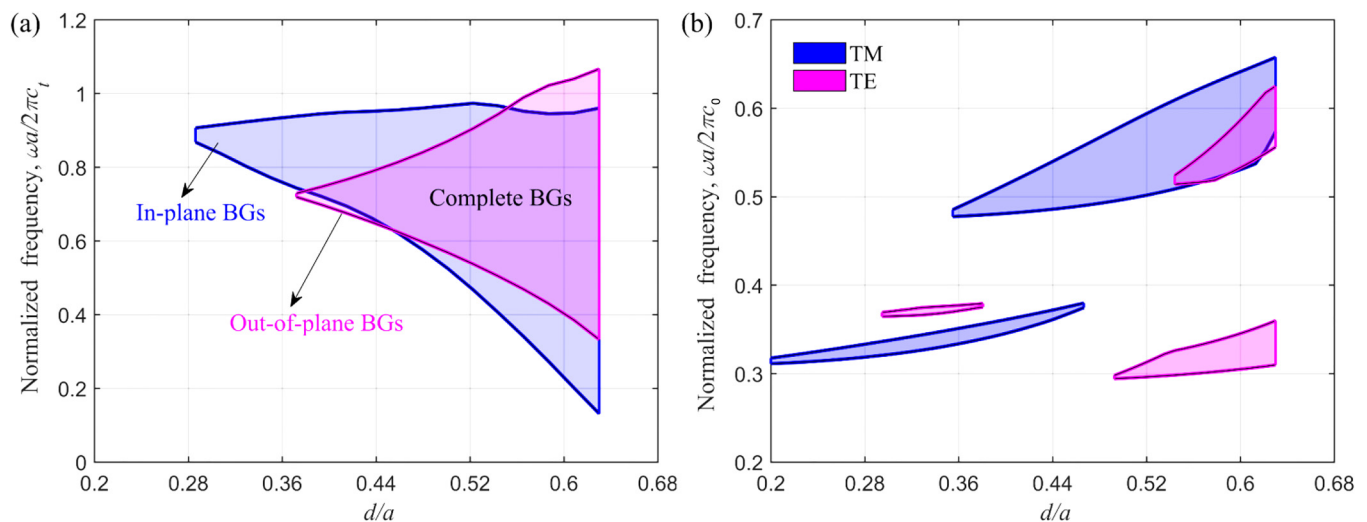
FIG. 5. Variation of (a) PnC and (b) PtC bandgaps with the geometrical parameter d/a, for $b/a = 0.58$ and $c/a = 0.32$.

to Fig. 3, similar features are observed: large bandgaps exist for a wide range of parameters, and the effect of the parameters on TE bandgaps is similar to the phononic case. However, two significant differences should be highlighted. One is that the regions of large bandgaps for TE and TM polarizations only overlap partially, thus reducing the complete bandgaps. Another difference is that the effect of the parameters on TM bandgaps lacks regularity.

Figure 5 illustrates the formation of large complete phoxonic bandgaps. Figures 5(a) and 5(b) show how the locations of phononic and photonic bandgaps vary with d/a, when $b/a = 0.58$ and $c/a = 0.32$ are fixed. In-plane (or TM) and out-of-plane (or TE) bandgaps are represented by blue and magenta regions, respectively. Complete bandgaps appear when they overlap. Comparatively, Fig. 5(b) shows a much more barren terrain.

IV. PHOXONIC CRYSTAL CAVITY DEFECT MODES

Once large complete phononic and photonic bandgaps have been achieved simultaneously, a phoxonic defect cavity can be introduced. The lattice constant a is fixed as 875 nm, for optical operation around $\lambda = 1550$ nm in silicon. A 7×7 super-cell provides a good compromise between accuracy of the results and reasonable computation time.[6] As shown in Fig. 6(d), the defect cavity is introduced by filling one cross-like hole in the center of the super-cell with silicon, inducing simultaneous photonic and phononic cavity modes. Owing to the large complete bandgaps, the phoxonic structure prevents photonic defect modes from moving out of the frequency bandgaps even under strong modulation, which is required for the design of acousto-optic coupling devices. The acoustic and optical eigenfrequencies and eigenvectors of the defective super-cell are calculated by FEM. The dispersion curves for photonic and phononic defect modes in the bandgap range are shown in Fig. 6.

The phononic and photonic dispersion relations are depicted only along the ΓX direction of the irreducible Brillouin zone, since

the bands associated with defect flat modes are flat and independent of the wave vector. One can notice that some new flatbands are born inside both phononic and photonic bandgaps after introduction of the defect cavity into the super-cell. The flat in-plane defect bands include 11 phononic bands (labeled with a, b, c, d, e, f, g, h, l, m, and n) in Fig. 6(a), 3 TE photonic bands (labeled α, β, and γ) in Fig. 6(b), and 3 TM photonic bands (α′, β′, and γ′) in Fig. 6(c). It is worth mentioning that these six photonic defect bands all occur within the complete photonic bandgap.

The modal shapes of the phononic cavity modes, magnified in the center of the structure, and the photonic modal shapes are displayed using displacements and electromagnetic fields in Figs. 6(e)–6(g), respectively. The displacements are highly localized in the cavity region. The electromagnetic fields also show a high confinement inside the cavity. We notice that among the 11 phononic modes, three pairs are degenerate (b and c, g and h, m and n). The same observation is also made for photonic TE modes α and β. The occurrence of degenerate modes can be explained by the cubic symmetry of silicon combined with the spatial symmetry of the structure.

The symmetry of the phononic modes is indeed one of the key factors governing the acousto-optic coupling strength. Following Ref. 5, modes are classified as odd (o) or even (e) with respect to the two symmetry axes P and P′ shown in Fig. 6(d). Both modes d and f have ee symmetry. In details, the vibration of mode d is a stretch-contract motion where the cavity stretches along symmetry axis P while it contracts along symmetry axis P′, and the extension–contraction state alternates once during every acoustic period. Mode f is a breathing mode that displays a breathing motion without too much distortion of the cavity shape. Moreover, the photonic TM modes α′ and β′ have ee symmetry, whereas modes γ and γ′ have oo symmetry. The degenerate photonic TE modes α and β have neither ee nor oo symmetry since they are a mixture; they can be obtained from one another by 90° clockwise
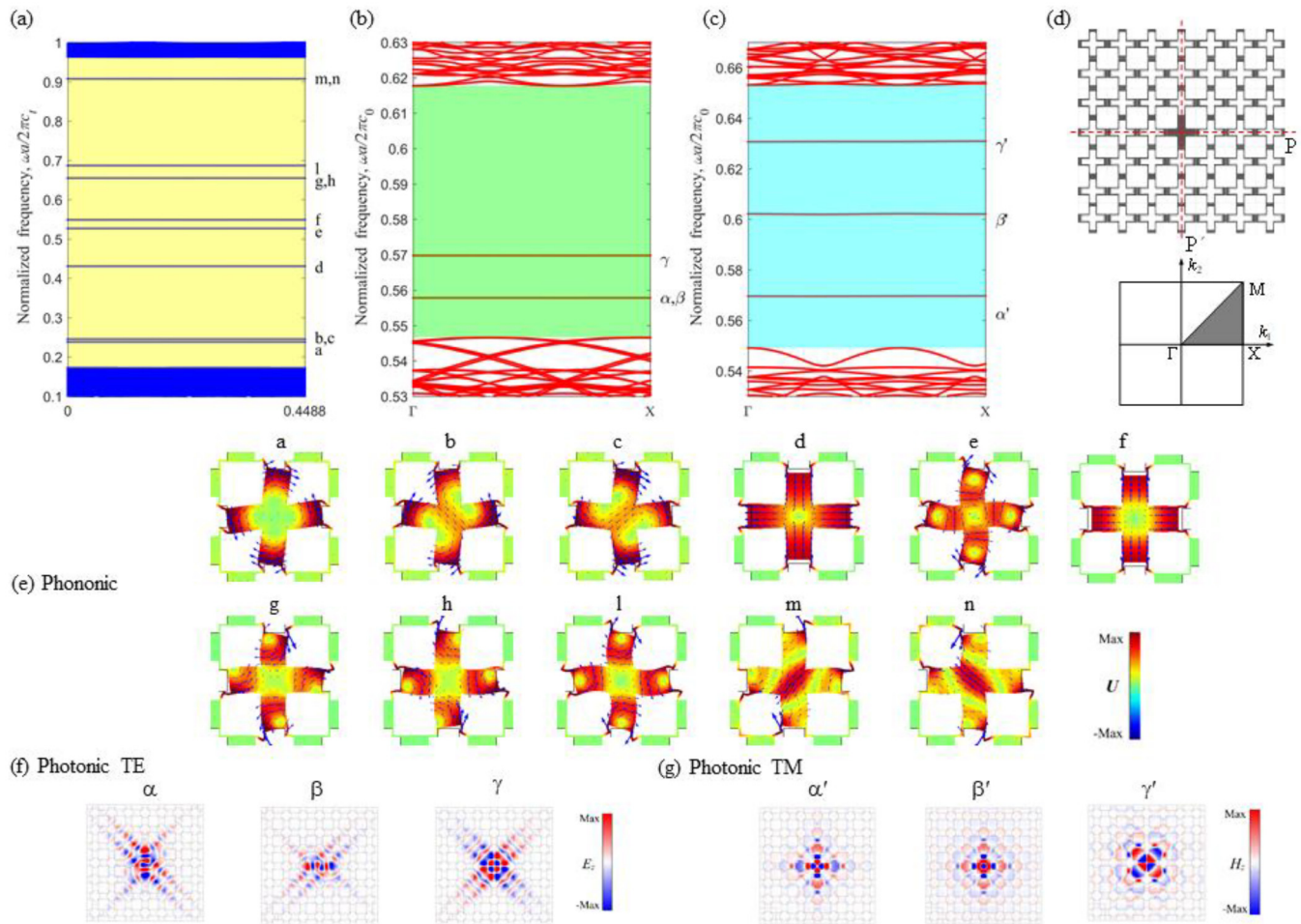
FIG. 6. Dispersion curves of (a) PnC, (b) TE PtC, and (c) TM PtC cavity modes. Eleven PnC defect bands, three TE PtC defect bands, and three TM PtC defect bands appear in bandgaps when the wave vector varies along the direction ΓX of the first Brillouin zone. (d) The 7 × 7 super-cell structure model and the irreducible Brillouin zone. (e) Displacement field distribution of the defect PnC modes corresponding to the defect bands in (a). (f) Electric field distribution in the z direction (E_z) of the defect TE PtC modes corresponding to the defect bands in (b). (g) Magnetic field distribution in the z direction (Hz) of the defect TM PtC modes corresponding to the defect bands in (c).

and anticlockwise rotations, respectively. Moreover, compared with the other symmetries of phononic modes, ee symmetric phononic modes have a stronger effect on the AO coupling.[10] Hence, we focus on the AO coupling with modes d and f in the following.

V. ACOUSTO-OPTIC COUPLING STRENGTH

The frequencies of the photonic TE and TM defect modes sustain a modulation around their initial values with a strength given by the magnitude of the acoustic strain inside the cavity, when that cavity is submitted to a periodic acoustic deformation. The frequency modulation results from the sinusoidal variation of the permittivity that is induced by the acoustic wave perturbation. Two mechanisms are responsible for it: (1) The moving interface (MI) effect[45] or permittivity variation caused by the moving of

the interfaces and (2) The photoelastic (PE) effect[46] or bulk permittivity variation induced by the strain field. Both effects are taken into consideration in the following calculations.

For Pockels effects, the variation of the relative permittivity $\Delta \varepsilon_{ij}$ is determined by the strain distribution considered frozen in time. $\Delta \varepsilon_{ij}$ are given for silicon by[47]

$$\Delta \varepsilon_{11} = -(p_{11}S_1 + p_{12}S_2), \quad \Delta \varepsilon_{22} = -(p_{12}S_1 + p_{11}S_2),$$
$$\Delta \varepsilon_{33} = -p_{12}(S_1 + S_2), \quad \Delta \varepsilon_{12} = \Delta \varepsilon_{21} = -p_{44}S_6, \quad (2)$$
$$\Delta \varepsilon_{13} = \Delta \varepsilon_{23} = \Delta \varepsilon_{31} = \Delta \varepsilon_{32} = 0,$$

where p_{ij} denote the photoelastic constants and S_i are the acoustic strains written in Voigt notation. For silicon, $p_{11} = -0.1$, $p_{12} = 0.01$,

and $p_{44} = -0.051$.[48] Thus, the symmetry of the strain field of the acoustic modes are inherited by the permittivity variation.

A. Coupling with phononic breathing mode f

Generally, the acousto-optic coupling strength is measured by the normalized optical frequency shift induced by a realistic acoustic wave perturbation. The maximum of the deformation u_{max} induced by acoustic wave perturbation is fixed as 1% of the lattice constant a, i.e., $u_{max} = 0.01a$, which is a reasonable choice that does not exceed strength limit of the material. Figure 7 displays the optical frequency modulations induced by the phononic breathing mode f during one acoustic period ($0 < \Omega t < 2\pi$) with the acoustic angular frequency Ω and time t, which is obtained by FEM. The contributions of the PE effect and MI effect are both illustrated. Whether for PE effect or MI effect, the modulations all display a sine function behavior representing linear coupling; in other words, it corresponds to one-phonon absorption and emission process by a photon. Specially, the degenerate photonic TE modes α and β display a complete synchronized modulation. The contribution of PE and MI can be in-phase and out-of-phase. In most cases, the MI effect is dominant except for the phononic TM mode γ'. The coupling for modes α, β, α', and β' is obviously larger than for the other two modes γ and γ'. The reason is that for the former, the electromagnetic field mainly distributes in the silicon area, whereas for the latter, it distributes in both silicon and hole areas. Moreover, the deformation induced by acoustic wave only affects silicon. The fact that the electromagnetic field and the displacement field highly overlap certainly enhances the coupling strength.

The acousto-optic coupling can also be evaluated from perturbation theory. The maximum deformation is chosen as the perturbation parameter. Based on first-order perturbation theory, the equation for non-degenerate phononic modes corresponding to one-phonon processes is derived as[45]

$$\Delta\omega^{(1)} = -\frac{\omega_0}{2} \frac{\langle E|(\Delta\varepsilon_{PE} + \Delta\varepsilon_{MI})|E\rangle}{\langle E|\varepsilon|E\rangle}, \tag{3}$$

where $\langle E|\varepsilon|E\rangle = \int \varepsilon|E|^2 dS$.

The PE contribution has a different form for different polarizations of the phononic mode. For the TM polarization,

$$\langle E|\Delta\varepsilon_{PE}|E\rangle = -\varepsilon_0 n^4 \int [2\mathrm{Re}\{E_x^* E_y\}p_{44}S_{xy}$$
$$+|E_x|^2(p_{11}S_{xx} + p_{12}S_{yy}) + |E_y|^2(p_{11}S_{yy} + p_{12}S_{xx})]dS, \tag{4}$$

where n is the refractive index. Re denotes taking the real part. Superscript $*$ represents conjugation. For the TE polarization,

$$\langle E|\Delta\varepsilon_{PE}|E\rangle = -\varepsilon_0 n^4 \int |E_z|^2 p_{12}(S_{xx} + S_{yy})dS. \tag{5}$$

The MI contribution of the PxC is given by

$$\langle E|\Delta\varepsilon_{MI}|E\rangle = \int (\mathbf{U} \cdot \mathbf{n})(\Delta\varepsilon \cdot \mathbf{E}_\parallel^2 - \Delta\varepsilon^{-1} \cdot \mathbf{D}_\perp^2)dl, \tag{6}$$

where $\mathbf{U}$ is the modal displacement field. A maximum of the deformation $u_{max} = \max(\mathbf{U})$ is defined as above. $\mathbf{n}$ is the outward
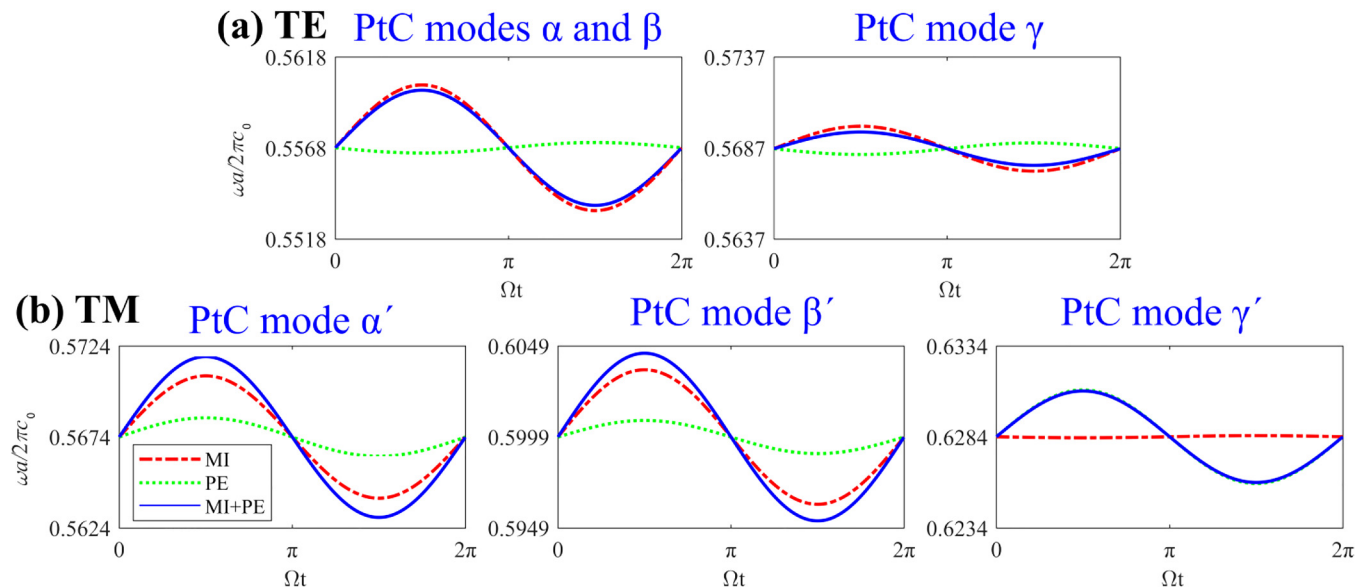

FIG. 7. Optical frequency modulation of (a) TE modes α, β, and γ and (b) TM modes α', β', and γ', with reduced frequency during one period of PnC breathing mode f. The moving interfaces (MI, red dashed lines), the photoelastic (PE, green dotted lines), and the full acousto-optic coupling (PE + MI, blue solid lines) are represented separately.

normal unit vector of the surface. **E** and **D** denote electric field and electric displacement field, respectively. The subscripts $\parallel$ and $\perp$ represent the components parallel and perpendicular to the interface between two dielectric materials, respectively. In our case, $\Delta\varepsilon = \varepsilon_{Si} - \varepsilon_{air}$ and $\Delta\varepsilon^{-1} = \varepsilon_{Si}^{-1} - \varepsilon_{air}^{-1}$.

For the two degenerate modes α and β, the frequency shift of a twofold degeneracy is obtained by degenerate perturbation theory,[41]

$$\Delta\omega^{(1)\pm} = \omega_0 \left[-\frac{\Gamma_{11}+\Gamma_{22}}{4} \pm \frac{1}{4}\sqrt{(\Gamma_{11}-\Gamma_{22})^2 + 4\Gamma_{12}\Gamma_{21}} \right], \quad (7)$$

where

$$\Gamma_{ij} = \frac{\langle E_i|\Delta\varepsilon|E_j\rangle}{\sqrt{\langle E_i|\varepsilon|E_i\rangle\langle E_j|\varepsilon|E_j\rangle}}. \quad (8)$$

This explicit expression can be derived based on Eqs. (4)–(6). E_1 and E_2 denote the electric fields of the degenerate modes, and $\Delta\omega^{(1)+}$ and $\Delta\omega^{(1)-}$ represent their frequency shifts.

The normalized frequency shifts ($\Delta\omega a/2\pi c_0$) obtained by perturbation theory are listed in Table II and agree well with the amplitude of the modulations in Fig. 7. A symmetry analysis further clarifies the result of perturbation theory. Because the deformation of the phononic breathing mode f in x and y directions is in-phase, the superposition of the integral in both directions is enhanced whatever the symmetry of the photonic mode. Linear coupling is absolutely dominant. For photonic degenerate modes α and β, $\Gamma_{11} = \Gamma_{22}$ and $\Gamma_{ij} = 0$ ($i \neq j$) because of rotational symmetry, which results in a synchronized modulation according to Eq. (7). It is noteworthy that the degenerate perturbation theory can be reduced to the non-degenerate perturbation theory when $\Gamma_{ij} = 0$ ($i \neq j$).

B. Coupling with phononic extension–contraction mode d

The optical frequency modulations of the six photonic defect modes coupled with phononic extension–contraction mode d are shown in Fig. 8. The modulation of the degenerate mode pair α and β still shows a sine function behavior; however, it is not synchronized, just as listed in Table II. This fact can be explained according to Eq. (7): we have $\Gamma_{11} = -\Gamma_{22}$ and $\Gamma_{ij} \neq 0$ ($i \neq j$); therefore, the modulations have opposite signs. Nevertheless, the other four photonic modes, γ, α', β',

TABLE II. Normalized frequency shift ($\times 10^{-3}$) of linear coupling obtained by first-order perturbation theory.

PtC modes	$\frac{\Delta\omega_{PE}a}{2\pi c_0}$	$\frac{\Delta\omega_{MI}a}{2\pi c_0}$	$\frac{\Delta\omega_{PE\&MI}a}{2\pi c_0}$
	Induced by the breathing mode f		
TE α	−0.288 61	3.3206	3.0320
TE β	−0.288 65	3.3206	3.0320
TE γ	−0.300 14	1.1909	0.890 73
TM α'	1.2041	3.3670	4.5711
TM β'	0.855 70	3.6800	4.5357
TM γ'	2.4520	−0.306 05	2.1460
	Induced by the extension–contraction mode d		
TE α	−0.057 357	3.2933	3.3506
TE β	0.057 357	−3.2933	−3.3506

and γ', show a squared sine function behavior. The reasons are analyzed as follows: The phononic extension–contraction mode d has out-of-phase deformation in x and y directions. These four photonic modes all have either ee or oo symmetry so that the term $|E|^2$ always has an ee symmetry. The integrals in the x and y directions cancel each other according to Eqs. (4)–(6). As a result, between each one of these four photonic modes and phononic mode d, linear coupling vanishes, and quadratic coupling is dominant over higher-order nonlinear effect. It is worth noting that quadratic coupling though weak has been proposed as a means for realizing quantum nondemolition (QND) measurement of the phonon number because of the square dependence with the motion displacement.[49–51]

In order to distinguish whether coupling is linear or quadratic, we further investigate the dependence of acousto-optic cavity coupling on the acoustic displacement by FEM. The normalized frequency shift of PE and MI as a function of the maximum of the deformation u_{max} is depicted in Fig. 9. Normalized frequencies of modes α and β both shift proportionally to the maximum of the deformation. Thus, these acousto-optic couplings are linear. Furthermore, for $u_{max}/u_0 = 1$, the linear coupling hypothesis agrees with the conclusion drawn by the perturbation theory, which is shown by optical frequency modulation amplitude in Fig. 8(a) and is also listed in Table II. In contrast, for the PE effect of modes γ, α', β' and γ', and the MI effect of γ, α' and β', normalized frequencies shift in proportion to the square of the maximum of the deformation. Therefore, these acousto-optic couplings are quadratic. Only the coupling for MI effect of mode γ' doesn't show a good linear or quadratic coupling. This may be caused by calculation errors, which are brought by two aspects: one is the weak coupling strength since the frequency shift is an order of magnitude smaller than other optical modes. The other is that the accurate calculation of MI effect requires a highly dense mesh in the boundary region to capture small deformation. Furthermore, as show in Fig. 9 and Fig. 8(b), the curves are close to that of quadratic coupling, and its PE effect behaves as quadratic coupling. Therefore the coupling for MI effect of mode γ' can still be considered as quadratic coupling.

Based on second-order perturbation theory, the equation for non-degenerate phononic modes corresponding to two-phonon processes is derived as[41]

$$\Delta\omega_i^{(2)} = \frac{3}{8}\omega_i^{(0)} \left| \frac{\langle E_i^{(0)}|\Delta\varepsilon_{PE} + \Delta\varepsilon_{MI}|E_i^{(0)}\rangle}{\langle E_i^{(0)}|\varepsilon^{(0)}|E_i^{(0)}\rangle} \right|^2$$
$$- \frac{1}{2}\sum_{j\neq i}\sum_{k=1}^{d_j} \frac{\omega_i^{(0)^3}}{\omega_j^{(0)^2} - \omega_i^{(0)^2}} \frac{\left|\langle E_{j,k}^{(0)}|\Delta\varepsilon_{PE} + \Delta\varepsilon_{MI}|E_i^{(0)}\rangle\right|^2}{\langle E_j^{(0)}|\varepsilon^{(0)}|E_j^{(0)}\rangle\langle E_i^{(0)}|\varepsilon^{(0)}|E_i^{(0)}\rangle}, \quad (9)$$

whereas for twofold degenerated modes,[41]

$$\Delta\omega_i^{(2)\pm} = \pm\frac{3}{8}\omega_i^{(0)} \left| \frac{\langle E_i^{(0)\pm}|\Delta\varepsilon_{PE} + \Delta\varepsilon_{MI}|E_i^{(0)\pm}\rangle}{\langle E_i^{(0)\pm}|\varepsilon^{(0)}|E_i^{(0)\pm}\rangle} \right|^2$$
$$- \frac{1}{2}\sum_{j\neq i}\sum_{k=1}^{d_j} \frac{\omega_i^{(0)^3}}{\omega_j^{(0)^2} - \omega_i^{(0)^2}} \frac{\left|\langle E_{j,k}^{(0)}|\Delta\varepsilon_{PE} + \Delta\varepsilon_{MI}|E_i^{(0)\pm}\rangle\right|^2}{\langle E_j^{(0)}|\varepsilon^{(0)}|E_j^{(0)}\rangle\langle E_i^{(0)\pm}|\varepsilon^{(0)}|E_i^{(0)\pm}\rangle}, \quad (10)$$
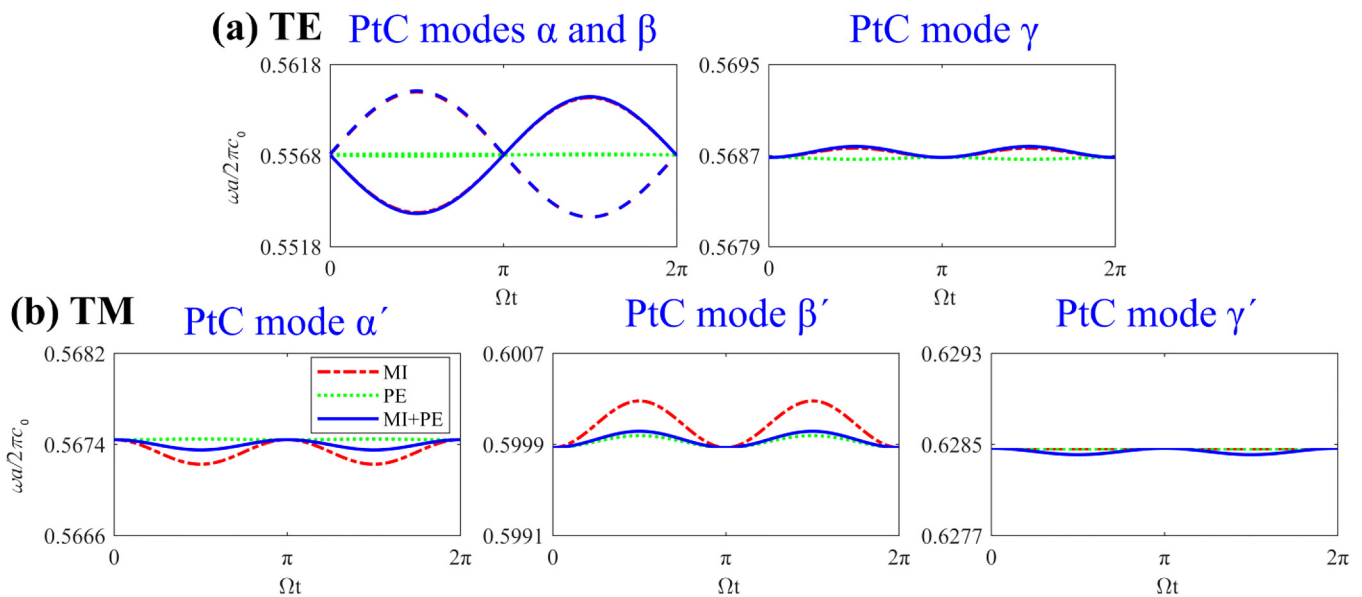
FIG. 8. Optical frequency modulation of (a) TE modes α, β, and γ and (b) TM modes α′, β′, and γ′, with normalized frequency during one period of PnC extension–contraction mode d. The moving interfaces (MI, red dashed lines), the photoelastic (PE, green dotted lines), and the full acousto-optic coupling (PE + MI, blue solid lines) are represented separately.

where photonic mode j has different frequency with ω_i. In general, only those modes with frequency close to ω_i and its electric field are taken into consideration.

Furthermore, Table III lists the normalized frequency shifts of quadratic coupling obtained by FEM and second-order perturbation theory. It is worth noting that the second-order perturbation theory has a large error compared with FEM in this case. Meanwhile, the FEM results depicted in Fig. 9 have good linear and quadratic effects, so the FEM results are reliable. Accordingly, the quadratic coupling results obtained by the second-order perturbation theory is regarded as unreliable.

C. Coupling rates relative to zero-point motion

In a quantum mechanical approach, the acousto-optic coupling strength is quantified by the frequency shift imparted by the zero-point motion of the mechanical resonator.[1,2,52–55] For linear coupling, $g^{(1)} = g' x_{\mathrm{zpf}}$. For quadratic coupling, $g^{(2)} = g'' x_{\mathrm{zpf}}^2$, where g' and g'' denote the coupling coefficients and $x_{\mathrm{zpf}} = \sqrt{\hbar/(2 m_{\mathrm{eff}} \Omega)}$ is the zero-point motion amplitude of the mechanical resonator, where $m_{\mathrm{eff}} = \int \rho (\mathbf{U}/u_{\mathrm{max}})^2 \mathrm{d}V$ represents the effective motional mass and Ω is the angular frequency of the acoustic mode. Since the PnC defect modes are all in-plane modes in our 2D model, the
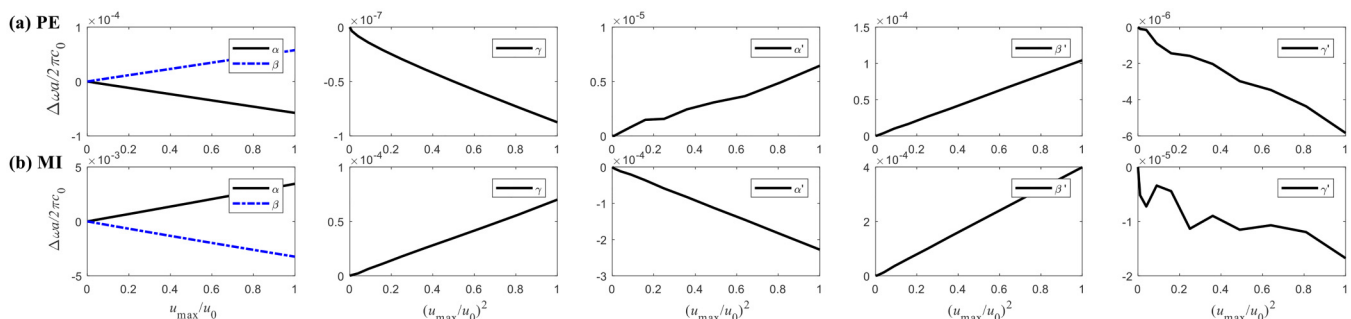

FIG. 9. Optical normalized frequencies shift as a function of the maximum of the deformation induced by acoustic extension–contraction mode d. (a) PE and (b) MI. The results are calculated by FEM, where $u_0 = 0.01a$ is fixed.

TABLE III. Comparison of the normalized frequency shifts of quadratic coupling obtained by either FEM or second-order perturbation theory.

Nromalized frequency shift $\Delta\omega a/ 2\pi c_0 (\times 10^{-3})$	$\frac{\Delta\omega_{PE} a}{2\pi c_0}$		$\frac{\Delta\omega_{MI} a}{2\pi c_0}$		$\frac{\Delta\omega_{PE\&MI} a}{2\pi c_0}$	
PnC–PtC	FEM	Second perturbation	FEM	Second perturbation	FEM	Second perturbation
d–γ	−0.01686	−0.007 41	0.081 031	0.008 78	0.095 68	0.007 65
d–α′	0.005 591	−0.065	−0.2159	−0.555	−0.089 95	−0.220 58
d–β′	0.1052	0.083	0.4098	0.692	0.142 992	0.27 526
d–γ′	−0.054 93	−0.001 71	−0.004 89	−0.001 35	−0.056 02	−0.000 55
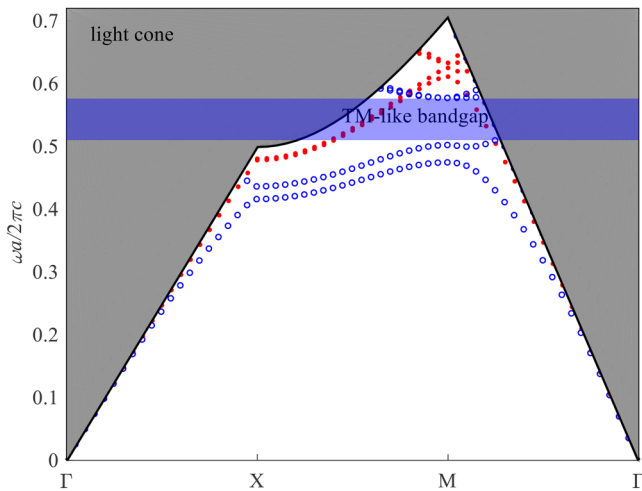
FIG. 10. Photonic dispersion curves of photonic slab with thickness of 220 nm.

effective motional mass can be rewritten as $m_{eff} = d_t \int \rho (U/u_{max})^2 dS$, where the thickness d_t is fixed as 220 nm. For the phononic breathing mode f, the effective motional mass and zero-point motion are 129 fg and 4.21 fm, respectively. As for the phononic extension–contraction mode d, the corresponding values are 178 fg and 4.04 fm, respectively. Comparing with a full 3D model with $m_{eff} = \int \rho (U/u_{max})^2 dV$, the relative errors for m_{eff} and x_{zpf} of the 2D model with $m_{eff} = d_t \int \rho (U/u_{max})^2 dS$ are smaller than 4%. Regarding computation times, they are reduced from 20 min to 58 s when replacing the 3D model by its 2D approximation. To demonstrate that the bandgaps also exist in 3D structures, photonic dispersion curves of the photonic slab are shown in Fig. 10. Below the light cone, a TM-like bandgap is clearly visible, which means the structure is practical to form defect modes or guide modes.

The coupling rates for six photonic defect modes coupled with phononic modes d and f obtained by FEM are shown in Table IV. Actually, these results can be obtained through a linear or quadratic transformation from the results of the linear or quadratic effect in Subsections V A and V B , respectively. Owing to its optical field being highly confined in silicon and overlapping efficiently with the displacement field, mode β′ has both maximum linear and quadratic coupling rates. The largest linear coupling rate $g^{(1)}/2\pi$ is

TABLE IV. Linear and quadratic coupling rates $g^{(1)}/2\pi$ and $g^{(2)}/2\pi$.

Mode pair PnC–PtC	PE	MI	PE and MI
	Linear coupling rate $g^{(1)}/2\pi$ (kHz)		
f–α	−47	526	478
f–β	−49	519	470
f–γ	−52	191	139
f–α′	174	555	729
f–β′	150	610	760
f–γ′	424	−18	404
d–α	9	−499	−490
d–β	−14	544	530
	Quadratic coupling rate $g^{(2)}/2\pi$ (Hz)		
d–γ	−0.0013	0.0064	0.0070
d–α′	0.0004	−0.0158	−0.0066
d–β′	0.0077	0.0300	0.0105
d–γ′	−0.0040	−0.0004	−0.0041

TABLE V. Comparison of maximum linear and quadratic coupling coefficients for the proposed model and some published structures.

Phoxonic crystal cavities	Coupling coefficients		Methods
	Linear coupling g' (GHz/nm)	Quadratic coupling g'' (MHz/nm²)	
Tilted membrane within an optical cavity[56]	0.0028	4.46	FEM and experiment
Fiber cavity[57]	3	20000	Experiment
Snowflake cavity[33]	17	n.a.	Experiment
Waveguide with air slot[58]	36	n.a.	FEM
Paddle cavity[40]	n.a.	400	FEM
This work	181	643	FEM

about 760 kHz for TM mode β' coupling with phononic breathing mode f. The largest quadratic coupling rate $g^{(2)}/2\pi$ is about 0.01 Hz for TM mode β' coupling with stretch-contract phononic mode d. The corresponding coupling coefficients g' and g'' are 181 GHz/nm and 643 MHz/nm^2, respectively. Table V lists maximum linear and quadratic coupling coefficients of some published structures and this work. It can be noted that the structure proposed in this work achieves the largest linear coupling coefficient and the second largest quadratic coupling coefficient. For optical modes coupled with acoustic modes of a few GHz, the coupling rate seems considerable. Nevertheless, the lower acoustic frequency, the larger the zero-point motion amplitude, and the larger the coupling rate, especially for quadratic coupling.

VI. CONCLUSION

A convex–concave 2D square lattice PxC was designed on the basis of a large phononic bandgap. Based on FEM and geometrical optimization, a comprehensive investigation of bandgaps has been performed. The results indicate that the convex–concave PxC can open simultaneously large complete photonic and phononic bandgaps, while at the same time preserving a simple topology. Moreover, large complete bandgaps can be achieved for a wide range of parameters. Maximum complete bandgaps of up to 90.7% for PnC and 11.5% for PtC are achieved after optimization. As a combination of convex and concave holes, the topology constituted by L-shaped connections and lumps is critical to induce dual bandgaps. The present study starts a new path for the design of PxCs. Moreover, with large complete bandgaps, the structure is a suitable choice to design a PxC cavity. Several defect phononic modes and photonic modes are obtained. Considering both the photoelastic and the moving interface mechanisms, the acousto-optic coupling was evaluated and the effect of symmetry on acousto-optic coupling was analyzed. The coupling strength was also investigated by FEM and first-order perturbation theory. The results of both methods are in good agreement for linear coupling, while second-order perturbation theory needs a correction to estimate quadratic coupling. Finally, the optomechanical coupling rate relative to zero-point motion was investigated by FEM. A photonic TM mode is found to have both the largest linear and quadratic coupling rates, in accordance with the optical field being strongly confined in the central silicon defect.

ACKNOWLEDGMENTS

AUTHOR DECLARATIONS

Conflict of Interest

The authors state no conflict of interest.

DATA AVAILABILITY

The data that support the findings of this study are available on request from the corresponding author. The data are not publicly available at this time.

REFERENCES

[1]M. Eichenfield, J. Chan, R. M. Camacho, K. J. Vahala, and O. Painter, Nature **462**(7269), 78 (2009).
[2]M. Eichenfield, R. Camacho, J. Chan, K. J. Vahala, and O. Painter, Nature **459**(7246), 550–555 (2009).
[3]S. Weis, R. Rivière, S. Deléglise, E. Gavartin, O. Arcizet, A. Schliesser, and T. Kippenberg, Science **330**(6010), 1520–1523 (2010).
[4]H. Ren, M. H. Matheny, G. S. MacCabe, J. Luo, H. Pfeifer, M. Mirhosseini, and O. Painter, Nat. Commun. **11**(1), 1–10 (2020).
[5]Y. Pennec, V. Laude, N. Papanikolaou, B. Djafari-Rouhani, M. Oudich, S. El Jallal, J. C. Beugnot, J. M. Escalante, and A. Martínez, Nanophotonics **3**(6), 413–440 (2014).
[6]Q. Rolland, M. Oudich, S. El-Jallal, S. Dupont, Y. Pennec, J. Gazalet, J. Kastelik, G. Lévêque, and B. Djafari-Rouhani, Appl. Phys. Lett. **101**(6), 061109 (2012).
[7]T. X. Ma, Y. S. Wang, Y. F. Wang, and X. X. Su, Opt. Express **21**(3), 2727–2732 (2013).
[8]H. W. Dong, Y. S. Wang, T. X. Ma, and X. X. Su, J. Opt. Soc. Am. B **31**(12), 2946–2955 (2014).
[9]V. Laude, J. C. Beugnot, S. Benchabane, Y. Pennec, B. Djafari Rouhani, N. Papanikolaou, J. M. Escalante, and A. Martinez, Opt. Express **19**(10), 9690–9698 (2011).
[10]S. El-Jallal, M. Oudich, Y. Pennec, B. Djafari-Rouhani, A. Makhoute, Q. Rolland, S. Dupont, and J. Gazalet, J. Phys.: Condens. Matter **26**(1), 015005 (2013).
[11]J. D. Joannopoulos, S. G. Johnson, J. N. Winn, and R. D. Meade, *Photonic Crystals: Molding the Flow of Light* (Princeton University Press, 2011).
[12]V. Laude, *Phononic Crystals: Artificial Crystals for Sonic, Acoustic, and Elastic Waves* (Walter de Gruyter GmbH & Co KG, 2015).
[13]M. I. Hussein, M. J. Leamy, and M. Ruzzene, Appl. Mech. Rev. **66**(4), 040802 (2014).
[14]J. Jin, X. Wang, L. Zhan, and H. Hu, Nanotechnol. Rev. **10**(1), 443–452 (2021).
[15]J. M. Escalante, A. Martínez, and V. Laude, J. Appl. Phys. **115**(6), 064302 (2014).
[16]R. Zhang, G. Chen, and J. Sun, Opt. Express **24**(12), 13051–13059 (2016).
[17]O. Sigmund and K. Hougaard, Phys. Rev. Lett. **100**(15), 153904 (2008).
[18]H. W. Dong, X. X. Su, and Y. S. Wang, J. Phys. D: Appl. Phys. **47**(15), 155301 (2014).
[19]Y. F. Li, X. D. Huang, and S. W. Zhou, Materials **9**(3), 186 (2016).
[20]O. R. Bilal and M. I. Hussein, Phys. Rev. E **84**(6), 065701 (2011).
[21]S. Jiang, H. P. Hu, and V. Laude, Phys. Status Solidi RRL **12**, 1700317 (2018).
[22]M. Maldovan and E. L. Thomas, Appl. Phys. Lett. **88**(25), 251907 (2006).
[23]S. Sadat-Saleh, S. Benchabane, F. I. Baida, M.-P. Bernal, and V. Laude, J. Appl. Phys. **106**(7), 074912 (2009).
[24]D. Bria, M. Assouar, M. Oudich, Y. Pennec, J. Vasseur, and B. Djafari-Rouhani, J. Appl. Phys. **109**(1), 014507 (2011).
[25]J. Bochmann, A. Vainsencher, D. D. Awschalom, and A. N. Cleland, Nat. Phys. **9**(11), 712 (2013).
[26]Q. Rolland, S. Dupont, J. Gazalet, J. C. Kastelik, Y. Pennec, B. Djafari-Rouhani, and V. Laude, Opt. Express **22**(13), 16288–16297 (2014).
[27]S. Mohammadi, A. A. Eftekhar, A. Khelif, and A. Adibi, Opt. Express **18**(9), 9164–9172 (2010).
[28]J. C. Hsu, T. Y. Lu, and T. R. Lin, Opt. Express **23**(20), 25814–25826 (2015).
[29]A. Korovin, Y. Pennec, and B. Djafari-Rouhani, Phys. Rev. B **96**(18), 184302 (2017).
[30]T. X. Ma, Y. S. Wang, and C. Z. Zhang, Opt. Commun. **312**, 68–72 (2014).

[31]H. W. Dong, Y. S. Wang, and C. Z. Zhang, IEEE Photonics J. **9**(2), 1–16 (2017).

[32]Z. J. Yu and X. K. Sun, Opt. Express **26**(2), 1255–1267 (2018).

[33]A. H. Safavi-Naeini, J. T. Hill, S. Meenehan, J. Chan, S. Gröblacher, and O. Painter, Phys. Rev. Lett. **112**(15), 153603 (2014).

[34]X. S. Qian, J. P. Li, M. H. Lu, Y. Q. Lu, and Y. F. Chen, J. Appl. Phys. **106**(4), 2059 (2009).

[35]I. Psarobas, N. Papanikolaou, N. Stefanou, B. Djafari-Rouhani, B. Bonello, and V. Laude, Phys. Rev. B **82**(17), 174303 (2010).

[36]O. Matsuda and O. Wright, J. Opt. Soc. Am. B **19**(12), 3028–3041 (2002).

[37]C. C. Chiu, W. M. Chen, K. W. Sung, and F. L. Hsiao, Opt. Express **25**(6), 6076 (2017).

[38]T. X. Ma, Y. S. Wang, and C. Zhang, Phys. Lett. A **381**(4), 323–329 (2016).

[39]B. Djafari-Rouhani, S. Eljallal, and P. Yan, C. R. Phys. **17**(5), 555–564 (2016).

[40]H. Kaviani, C. Healey, M. Wu, R. Ghobadi, A. Hryciw, and P. E. Barclay, Optica **2**(3), 271–274 (2015).

[41]A. El-Soussi, J. Gazalet, S. Dupont, and J. Kastelik, J. Opt. **21**(4), 045103 (2019).

[42]M. Aspelmeyer, T. J. Kippenberg, and F. Marquardt, Rev. Mod. Phys. **86**(4), 1391–1452 (2014).

[43]M. Born and E. Wolf, *Principles of Optics: Electromagnetic Theory of Propagation, Interference and Diffraction of Light*, 7th (expand) ed. (Publishing House of Electronics Industry, 2013).

[44]A. Yariv and P. Yeh, *Photonics: Optical Electronics in Modern Communications*, 6th ed. (Publishing House of Electronics Industry, 2014).

[45]S. G. Johnson, M. Ibanescu, M. Skorobogatiy, O. Weisberg, J. Joannopoulos, and Y. Fink, Phys. Rev. E **65**(6), 066611 (2002).

[46]A. Yariv and P. Yeh, *Optical Waves in Crystals* (Wiley, New York, 1984).

[47]P. T. Rakich, C. Reinke, R. Camacho, P. Davids, and Z. Wang, Phys. Rev. X **2**(1), 011008 (2012).

[48]D. K. Biegelsen, Phys. Rev. Lett. **32**(21), 1196 (1974).

[49]M. Ludwig, A. H. Safavi-Naeini, O. Painter, and F. Marquardt, Phys. Rev. Lett. **109**(6), 063601 (2012).

[50]S. R. Sathyamoorthy, L. Tornberg, A. F. Kockum, B. Q. Baragiola, J. Combes, C. M. Wilson, T. M. Stace, and G. Johansson, Phys. Rev. Lett. **112**(9), 093601 (2014).

[51]H. Miao, S. Danilishin, T. Corbitt, and Y. Chen, Phys. Rev. Lett. **103**(10), 100402 (2009).

[52]J. Chan, A. H. Safavi-Naeini, J. T. Hill, S. Meenehan, and O. Painter, Appl. Phys. Lett. **101**(8), 081115 (2012).

[53]J. Chan, T. M. Alegre, A. H. Safavi-Naeini, J. T. Hill, A. Krause, S. Gröblacher, M. Aspelmeyer, and O. Painter, Nature **478**(7367), 89–92 (2011).

[54]A. H. Safavi-Naeini, T. M. Alegre, J. Chan, M. Eichenfield, M. Winger, Q. Lin, J. T. Hill, D. E. Chang, and O. Painter, Nature **472**(7341), 69–73 (2011).

[55]M. Kalaee, T. K. Paraiso, H. Pfeifer, and O. Painter, Opt. Express **24**(19), 21308–21328 (2016).

[56]M. Karuza, M. Galassi, C. Biancofiore, C. Molinelli, R. Natali, P. Tombesi, G. Di Giuseppe, and D. Vitali, J. Opt. **15**(2), 025704 (2012).

[57]N. Flowers-Jacobs, S. Hoch, J. Sankey, A. Kashkanova, A. Jayich, C. Deutsch, J. Reichel, and J. Harris, Appl. Phys. Lett. **101**(22), 221109 (2012).

[58]A. Pitanti, J. M. Fink, A. H. Safavi-Naeini, J. T. Hill, C. U. Lei, A. Tredicucci, and O. Painter, Opt. Express **23**(3), 3196–3208 (2015).